Electronic Supplementary Material (ESI) for Chemical Communications.

Thermal Evolution of NASICON type Solid-state Electrolytes with Lithium at High Temperature via In-Situ Scanning Electron Microscopy

Shirin Kaboli[1], Gabriel Girard[1], Wen Zhu[1], Alina Gheorghe Nita[1], Chandramohan George[2], Michel L. Trudeau[1], Andrea Paolella[1]*

[1] Hydro-Québec's Center of Excellence in Transportation Electrification and Energy Storage, Varennes, Québec J3X 1S1, Canada

[2] Dyson School of Design Engineering, Imperial College London, SW7 2AZ, London, UK

[*]E-mail: paolella.andrea2@hydroquebec.com

Supporting Information

Experimental Methods

We conducted in-situ heating tests on Li-LATP and Li-LAGP sample assemblies in plane-view in a high-vacuum Schottky electron microscope (chamber pressure ~ 10^5 Pa at RT). The LATP pellet was very fragile and split into two halves during sample handling and insertion into the SEM. Half of the pellet was lost in the vacuum at the beginning of the experiment, revealing the Li foil under the LATP pellet in the top left of the movie (Movie S1). We monitored various dynamic phenomena in the Li ceramic pellet using continuous SE imaging. We presented the changes in surface chemistry after the reaction at the interface using post-mortem EDS and X-ray diffraction on the samples at RT. We also performed electron backscatter diffraction (EBSD) crystal orientation mapping on the pellets to map the grain boundary distributions.

Preparation of LAGP (or LATP) Pellet

A standard self-standing LAGP film was prepared by adding LAGP (MSE Supplies LLC.) or LATP (Toshima Manufacturing Co.) to a mixture of polyvinyl difluoride-hexafluoropropylene in dimethylformamide and tetrahydrofuran (THF) in a 1:1 v/v ratio. This coating was cast onto a polypropylene sheet (to prevent the film from sticking) and dried at 50 °C to evaporate the THF. Then, a flexible film was punched and annealed between two glass disks in a muffle furnace (Nabertherm) at 850 °C (900 °C for LATP) for 10 h in air. The density of the final thin LAGP (0.1 mm thickness) was approximately 80%, while the standard 1 mm thick LAGP was approximately 90%–95%. The XRD analysis of the pristine thin LAGP pellet can be found in [12]. Figure S3 shows the results of the EBSD orientation mapping on the LATP surface. The inverse pole figure (IPF) coloring map is shown in (A), and the grain size histogram is shown in (B). Figure S4 shows the secondary electron (SE) images of the surface morphology of the LAGP pellet with 0.1 mm thickness. EBSD orientation mapping could not be performed on LAGP owing to severe surface beam damage from 20 keV electron beam energy in the SEM.

We used a laminated Li metal with 0.2 wt% Al sheet (thickness: 40 μm; LTE-Hydro-Québec, Shawinigan, QC) with a melting point of ~180.5 °C. The Li sheets had a very thin (nanometer-

scale) organic residual coating on the top surface formed during the fabrication process. For each sample assembly, the pellet was placed onto the surface of the Li metal and pressed gently to ensure physical contact. Sample handling and surface preparation were performed in a dry room with a dew point of ~−53 °C to minimize moisture and surface contamination. All SEM observations were performed in a dry room. We did not perform any surface preparation on the Li foil-ceramic pellet sample assembly before SEM.

In-situ Heating Setup

The in-situ heating setup was designed and manufactured in-house (Hydro-Québec). Heating was performed by using a resistance furnace mounted on the SEM stage. We used Ni foils to protect the parts of the furnace in contact with the Li melt to avoid possible damage or contamination of the furnace. We used a chiller and liquid nitrogen cold trap to reduce sample contamination and cool the stage during the heating tests. **Figure S5** shows the sample and stage temperature profiles obtained during the experiments. For all heating tests, the temperature was increased from RT to 330 °C over 90 minutes. The furnace was turned off at a maximum temperature of 330 °C to prevent any possible damage to the SEM stage components. For temperature measurements, two thermocouples were used to continuously monitor the sample and stage temperatures. The estimated error in the sample temperature readings was approximately ±5 °C. The temperature was increased stepwise with a 30 minute holding time at each step to ensure a uniform temperature in the sample. For heating, we used a Eurotherm EPC3008 controller and iTools software (version 9.79). This software is equipped with an OPC scope acquisition module, which enables temperature control through the controller.

In-situ Imaging in SEM

We used a MIRA3 TESCAN SEM equipped with a standard EDS detector (Oxford Instruments) and a windowless extreme EDS detector (Oxford Instruments), which can detect Li, and a NordlysNano EBSD system. The large chamber of this microscope provides an ideal

platform for installing a heating module for in-situ heating experiments. The vacuum pressure inside the SEM chamber was ~10^{-5} Pa at RT and was increased up to ~8×10^{-3} Pa owing to the outgassing of the sample, furnace, and stage at high temperatures. We performed in-beam SE imaging at low magnification (wide view), beam energy of 4-5 keV, and operation distance of ~14–15 mm. EDS was performed at a beam energy of 10 keV. Imaging was performed in plane-view on the surface of the pellet in contact with the Li metal foil underneath the pellet. In these experiments, it was not possible to predict where the reaction would initiate; therefore, it was important to have a wide view of the entire pellet surface during heating to locate the reaction initiation zone. It was also useful to see part of the Li sample to observe the changes in Li close to the melting point as this usually induces reaction initiation at the interface. The time step between images was typically 2–30 s, depending on the kinetics of the changes in surface morphology as a function of temperature. The electron beam scanning time for each image was 2 s. After the tests, the images were used to construct movies to observe various dynamic phenomena in the sample. We used MATLAB computer programming to construct movies from the SEM images.

We also performed X-ray diffraction analysis using a Rigaku MiniFlex benchtop powder X-ray diffraction (XRD) instrument with a 12 h scan with rotation at 10-90° sample tilt. Note that the resolution of the XRD patterns were low due to the small quantity of the reaction products and severe topography of the surface resulting in low signal to noise ratio. Also, the post-mortem X-ray photoelectron spectroscopy (XPS) analysis to identify possible amorphous phases could not be used due to the severe topography of the reaction products after the experiments.

Thick LAGP (~1 mm thickness) In-situ Heating Test

Figure S6B shows a higher magnification SE image of Figure S6A with the particles formed during the Li-LAGP 1 mm thick reaction. Figure S6C-F shows the results of EDS mapping at four locations (spots 1-4). Spot 1 was selected on the LAGP pellet and showed a homogeneous distribution of Al (with minor segregation), Ge, and P (Figure S6C). Spots 2 and 3 show common segregation of Ge in areas depleted of P with a homogeneous distribution of Al (Figure S6 D, E), while P is segregated in spot 4 (Figure S6F). **Figure S7** shows the XRD spectrum of the Li-LAGP 1 mm thick sample. The high-intensity peaks correspond to the Ni substrate. The low-intensity peaks in the spectra correspond to possible new phases such as $Li_{22}Ge_5$, Li_2O, $LiAl_{0.983}Ge_{0.066}$, Li_3P, $AlPO_4$, and GeP_2O_7. Due to low intensity peaks, the accurate phase determination is difficult. Correlating the XRD spectrum with the EDS maps in Figure S6, there is a likely presence of $Li_{22}Ge_5$ (Ge-rich particles in Figure S6D and S6E), Li_2O (O-rich particles in Figure S6E, S6F), and Li_3P (P-rich particles in Figure S6E). Despite different thicknesses of LAGPs, the common decomposition products seem to be $Li_{22}Ge_5$ and Li_3P, as well as Li-Al-Ge alloys. In addition, we performed in-situ heating on a self-standing LAGP pellet without observing any side reactions (Figure S8).

Movie S1. Real-time observations of the Li-LATP 0.1 mm thick sample assembly during in-situ heating in SEM.

Movie S2. Real-time observations of the Li-LAGP 0.1 mm thick sample assembly during in-situ heating in SEM.

Movie S3. Real-time observations of the Li-LAGP 0.1 mm thick sample assembly during in-situ heating in SEM showing the fast kinetics of the Li-LAGP reaction and saturation of the secondary electron (SE) detector due to the infrared irradiation from the reaction.

Movie S4. Real-time observations of the Li-LAGP 1 mm thick sample assembly during in-situ heating in SEM.

Movie S5. Real-time observations of a Li metal foil during in-situ heating in SEM.

Figure S1. The results of X-ray diffraction (XRD) spectra at full 2-theta range for (A) Li-LATP (0.1 mm thick), (B) Li-LAGP (0.1 mm thick) and (C) Li-LAGP (1 mm thick). The red rectangle represents the range of 2-theta that was magnified and shown in Figures 3, 5, and 7 in the text.

Figure S2. The photos of Li-LAGP 1 mm thick sample assembly after cooling down to RT. (A) The photo was taken from the top surface. (B) The photo was taken after the LAGP pellet was flipped over to reveal the bottom surface. The bottom left corner is where the reaction started. The pellet was mechanically stable during heating with no visible cracking on the surface.

Figure S3. The results of electron backscatter diffraction (EBSD) orientation mapping on the LATP surface. (A) The inverse pole figure (IPF-Z) coloring map and (B) the grain size histogram.

Figure S4. The secondary electron (SE) images of the LAGP pellet with 0.1 mm thickness showing (A) an overview of the surface morphology and (B) nano-size grain structure.

Figure S5. The sample and stage temperature profiles for the in-situ heating experiments inside the scanning electron microscope (SEM) in this study.

Figure S6. Secondary electron (SE) imaging and post-mortem energy-dispersive spectroscopy (EDS) mapping of Li-LAGP 1 mm sample after the heating (A) SE image at low magnification, (B) higher magnification SE image from the reaction zone in (A), (C-F) EDS maps acquired from spots 1-4 in (B). Segregation of Ge and P are observed in (C-F).

Figure S7. Post-mortem X-ray powder diffraction (XRD) of Li-LAGP mm sample after heating. The XRD spectrum after a zoom-in and signal smoothing to observe the smaller peaks corresponding to the new phases formed during the Li-LAGP reaction.

Figure S8. Secondary electron (SE) images of the self-standing pellets with no contact with the Li metal during in-situ heating experiments. (A) LATP 0.1 mm thick pellet at RT, (B) LATP 0.1 mm thick pellet at 330 °C, (C) LAGP 0.1 mm thick pellet at RT and (D) LAGP 0.1 mm thick pellet at 330 °C. The self-standing pellets were stable in this temperature range and showed no cracking or change of surface morphology.

Figure S9. Secondary electron (SE) imaging and post-mortem energy-dispersive spectroscopy (EDS) mapping of Li metal before and after heating. (A) SE image at low magnification (from Movie S5), (B) higher magnification SE image from the center of the Li metal foil (indicated by a red square in (A)) at RT, (C) same area after heating to 330 °C and cool down to RT, (D) EDS maps acquired at RT and (E) post-mortem EDS maps acquired after heating to 330 °C and cool down to RT. O concentrations are high at the Li grain boundaries at RT but the entire surface oxidizes after heating above the Li metal melting point. C segregation after heating and cool down is a result of contamination deposition on the surface.

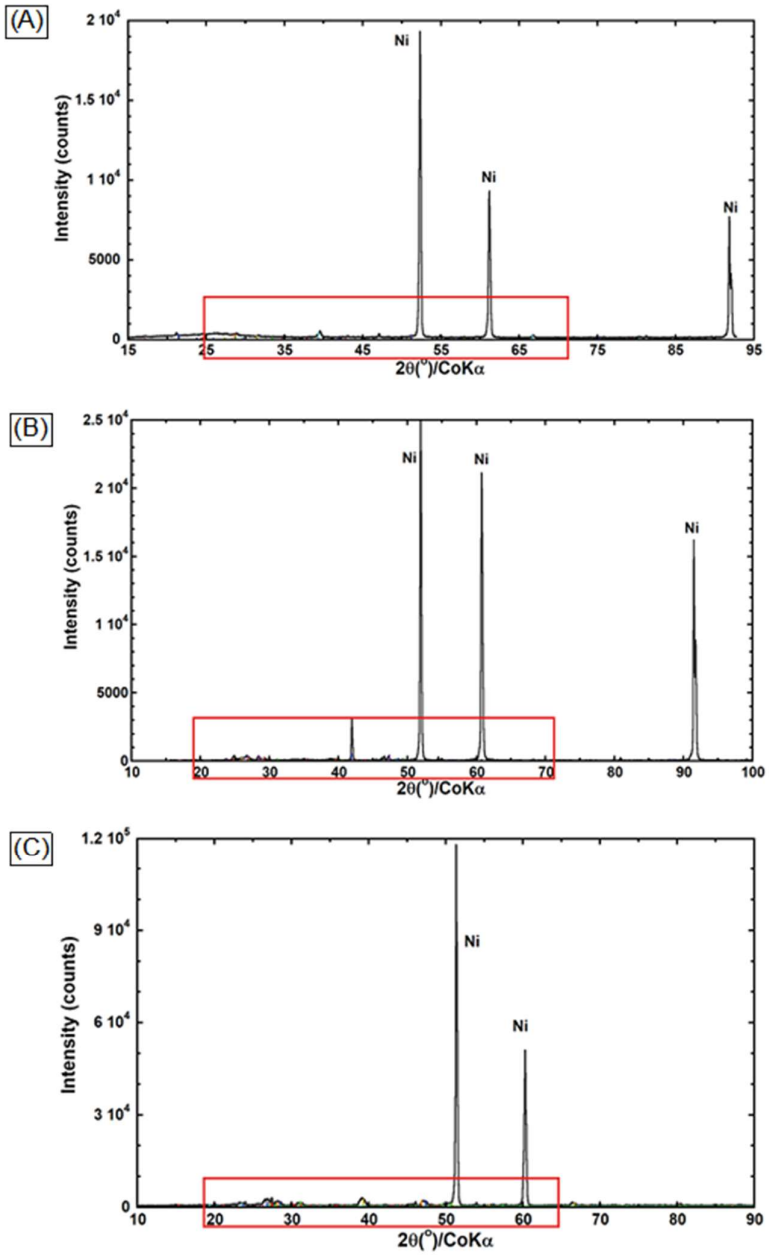

Figure S1. The results of X-ray diffraction (XRD) spectra at full 2-theta range for (A) Li-LATP (0.1 mm thick), (B) Li-LAGP (0.1 mm thick) and (C) Li-LAGP (1 mm thick). The red rectangle represents the range of 2-theta that was magnified and shown in Figures 3, 5, and S7 in the text.

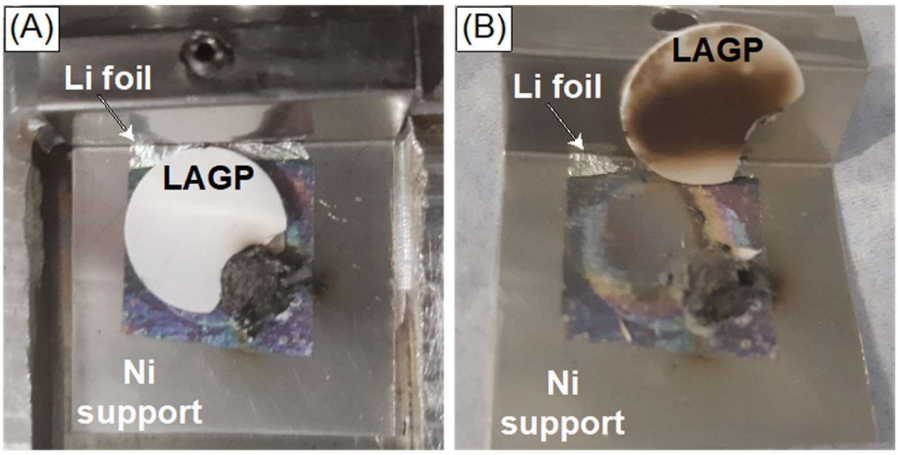

Figure S2. The photos of Li-LAGP 1 mm thick sample assembly after cooling down to RT. (A) The photo was taken from the top surface. (B) The photo was taken after the LAGP pellet was flipped over to reveal the bottom surface. The bottom left corner is where the reaction started. The pellet was mechanically stable during heating with no visible cracking on the surface.

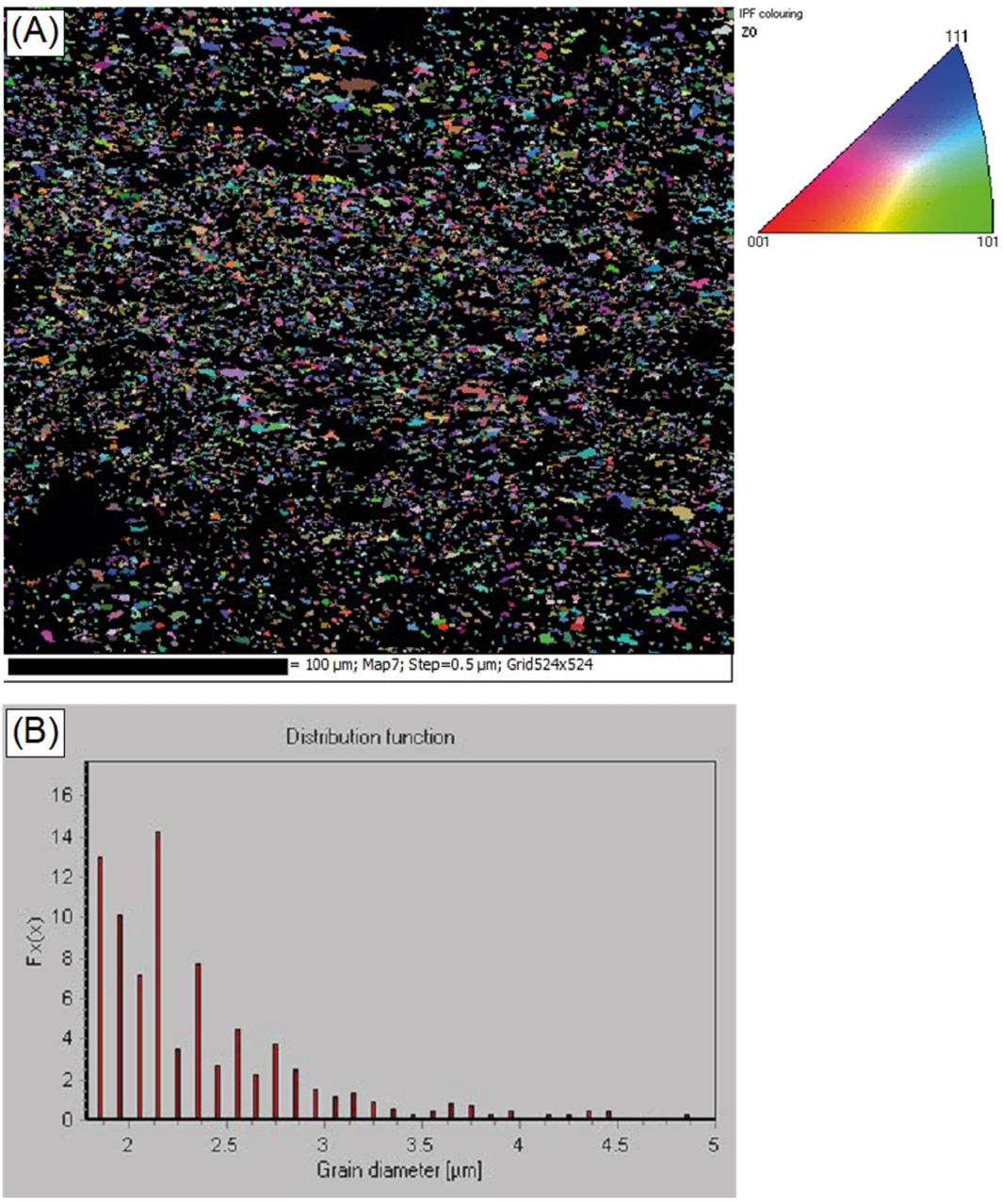

Figure S3. The results of electron backscatter diffraction (EBSD) orientation mapping on the LATP surface. (A) The inverse pole figure (IPF-Z) coloring map and (B) the grain size histogram.

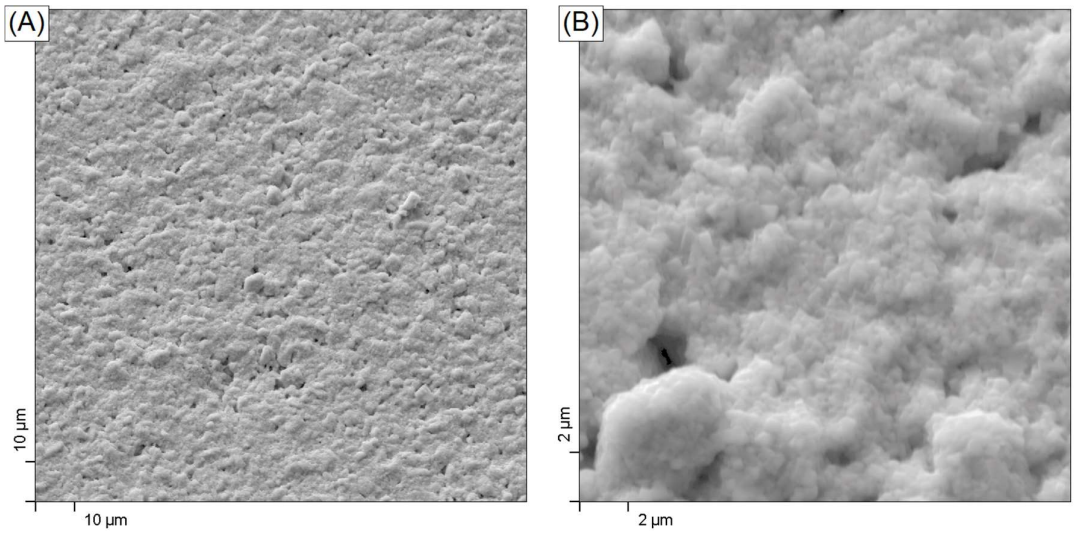

Figure S4. The secondary electron (SE) images of the LAGP pellet with 0.1 mm thickness showing (A) an overview of the surface morphology and (B) nano-size grain structure.

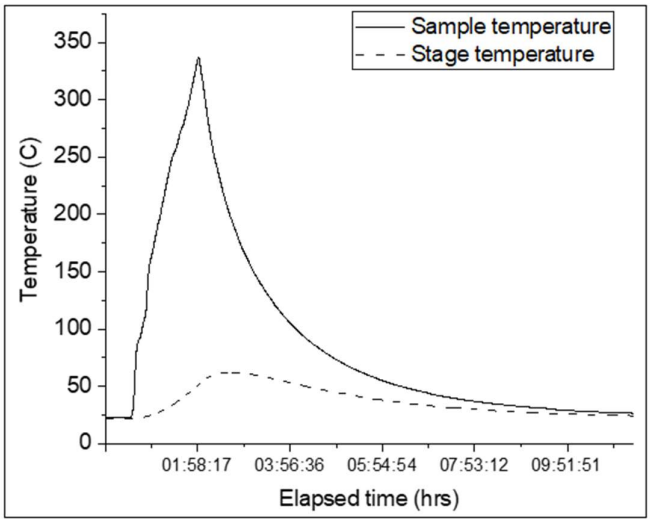

Figure S5. The sample and stage temperature profiles for the in-situ heating experiments inside the scanning electron microscope (SEM) in this study.

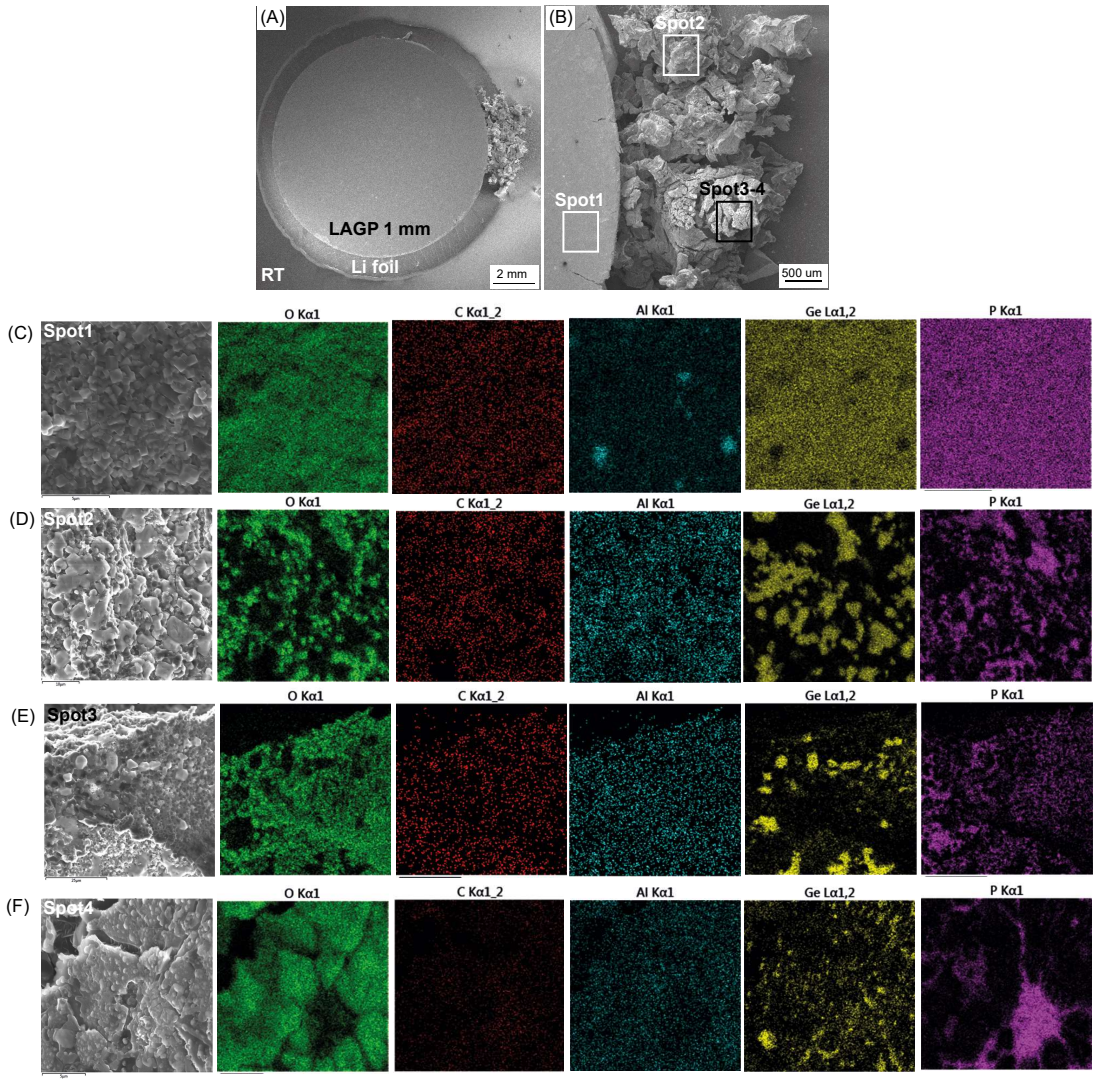

Figure S6. Secondary electron (SE) imaging and post-mortem energy-dispersive spectroscopy (EDS) mapping of Li-LAGP 1 mm sample after the heating (A) SE image at low magnification, (B) higher magnification SE image from the reaction zone in (A), (C-F) EDS maps acquired from spots 1-4 in (B). Segregation of Ge and P are observed in (C-F).

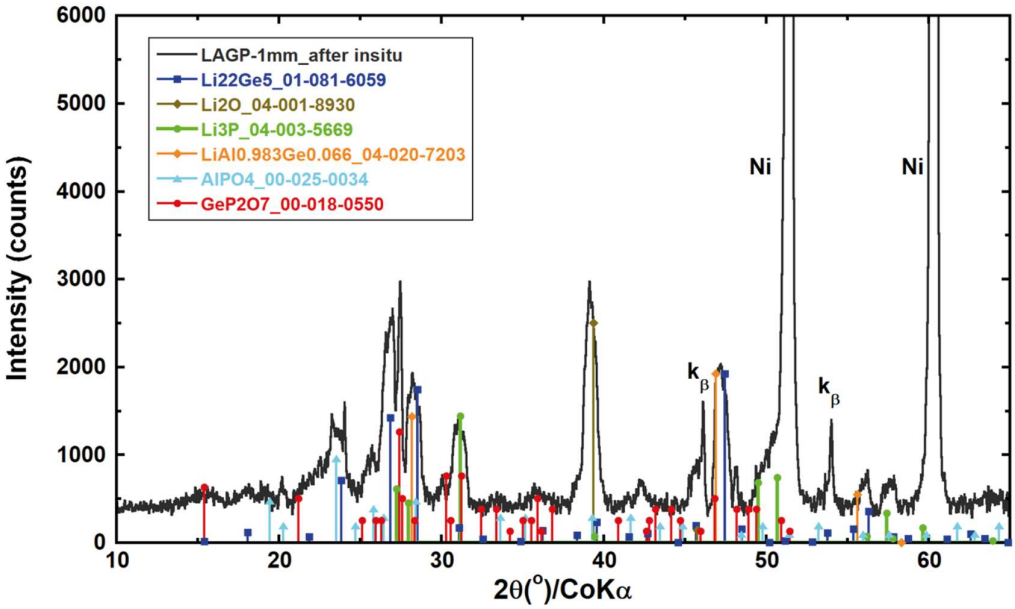

Figure S7. Post-mortem X-ray powder diffraction (XRD) of Li-LAGP mm sample after heating. The XRD spectrum after a zoom-in and signal smoothing to observe the smaller peaks corresponding to the new phases formed during the Li-LAGP reaction.

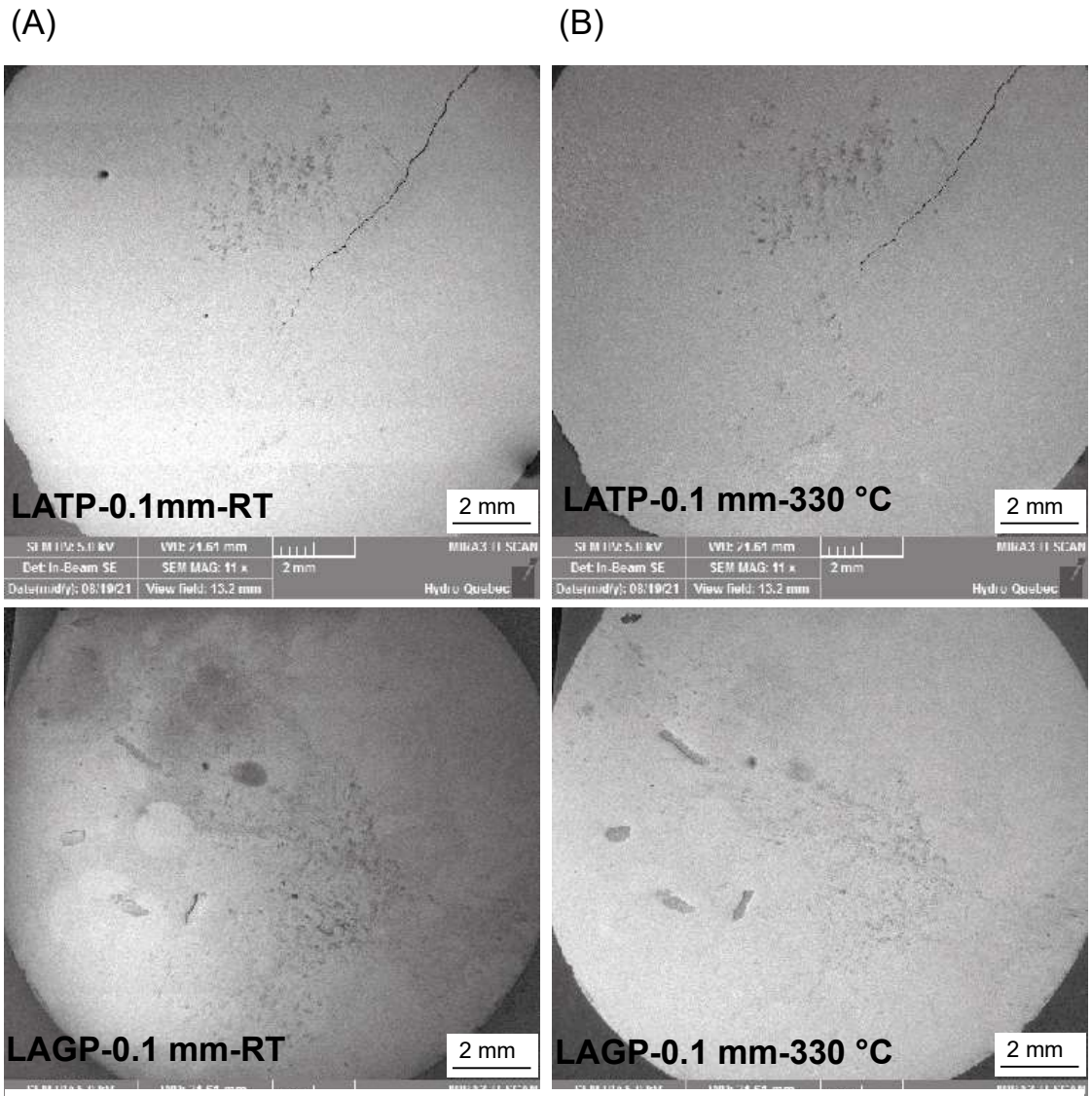

Figure S8. Secondary electron (SE) images of the self-standing pellets with no contact with Li metal during in-situ heating experiments. (A) LATP 0.1 mm thick pellet at RT, (B) LATP 0.1 mm thick pellet at 330 °C, (C) LAGP 0.1 mm thick pellet at RT and (D) LAGP 0.1 mm thick pellet at 330 °C. The self-standing pellets were stable in this temperature range and showed no cracking or change of surface morphology.

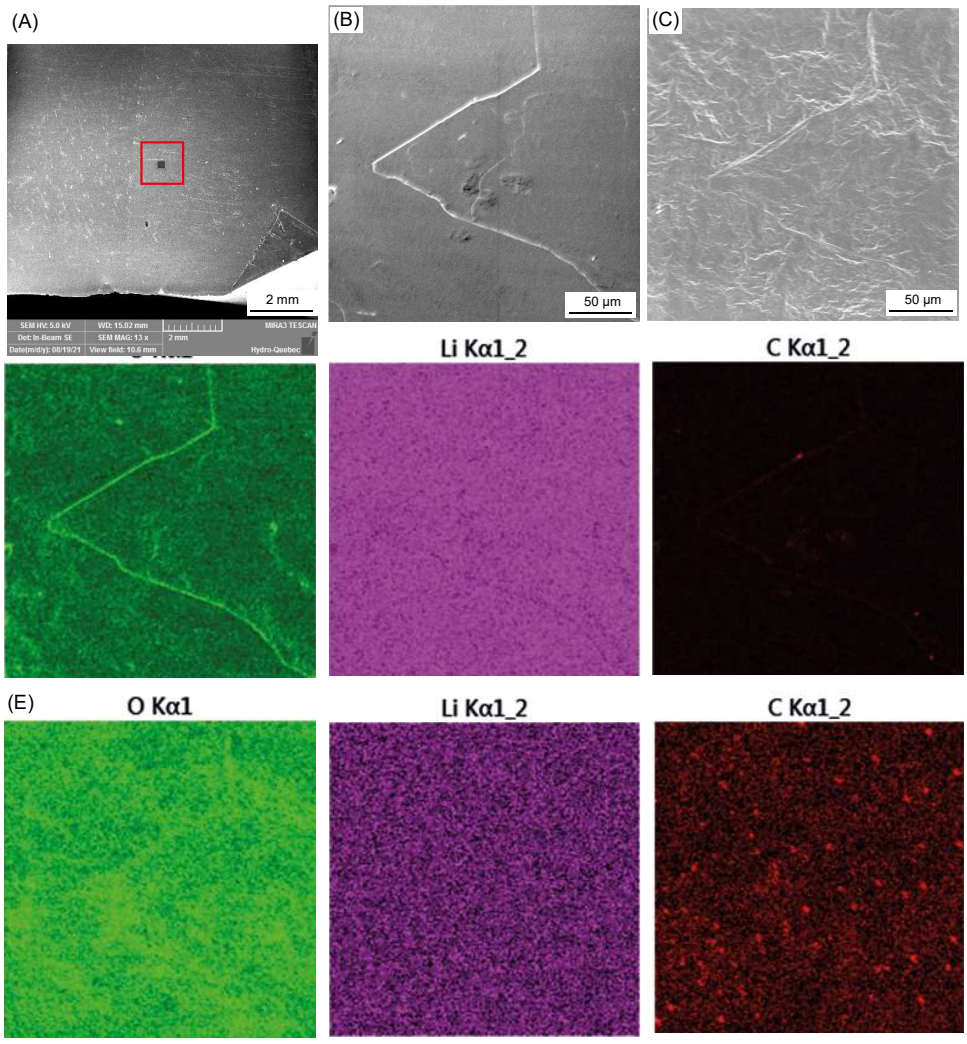

Figure S9. Secondary electron (SE) imaging and post-mortem energy-dispersive spectroscopy (EDS) mapping of Li metal before and after heating. (A) SE image at low magnification (from Movie S5), (B) higher magnification SE image from the center of the Li metal foil (indicated by a red square in (A)) at RT, (C) same area after heating to 330 °C and cool down to RT, (D) EDS maps acquired at RT and (E) post-mortem EDS maps acquired after heating to 330 °C and cool down to RT. O concentrations are high at the Li grain boundaries at RT but the entire surface oxidizes after heating above the Li metal melting point. C segregation after heating and cool down is a result of contamination deposition on the surface.

References

(1) Armand, M.; Tarascon, J. M. *Nature* **2008**, 451, (7179), 652-657.

(2) Tong, Z.; Wang, S.-B.; Liao, Y.-K.; Hu, S.-F.; Liu, R.-S. *ACS Applied Materials & Interfaces* **2020**, 12, (42), 47181-47196.

(3) Wang, L.; Li, J.; Lu, G.; Li, W.; Tao, Q.; Shi, C.; Jin, H.; Chen, G.; Wang, S. *Frontiers in Materials* **2020**, 7, (111).

(4) Zhao, W.; Yi, J.; He, P.; Zhou, H. *Electrochemical Energy Reviews* **2019**, 2, (4), 574-605.

(5) Yang, X.; Adair, K. R.; Gao, X.; Sun, X. *Energy & Environmental Science* **2021**, 14, (2), 643-671.

(6) Kim, K. J.; Balaish, M.; Wadaguchi, M.; Kong, L.; Rupp, J. L. M. *Advanced Energy Materials* **2021**, 11, (1), 2002689.

(7) DeWees, R.; Wang, H. *ChemSusChem* **2019**, 12, (16), 3713-3725.

(8) Hartmann, P.; Leichtweiss, T.; Busche, M. R.; Schneider, M.; Reich, M.; Sann, J.; Adelhelm, P.; Janek, J. *The Journal of Physical Chemistry C* **2013**, 117, (41), 21064-21074.

(9) He, L.; Sun, Q.; Chen, C.; Oh, J. A. S.; Sun, J.; Li, M.; Tu, W.; Zhou, H.; Zeng, K.; Lu, L. *ACS Applied Materials & Interfaces* **2019**, 11, (23), 20895-20904.

(10) Xiao, Y.; Wang, Y.; Bo, S.-H.; Kim, J. C.; Miara, L. J.; Ceder, G. *Nature Reviews Materials* **2020**, 5, (2), 105-126.

(11) Zhu, J.; Zhao, J.; Xiang, Y.; Lin, M.; Wang, H.; Zheng, B.; He, H.; Wu, Q.; Huang, J. Y.; Yang, Y. *Chemistry of Materials* **2020**, 32, (12), 4998-5008.

(12) Paolella, A.; Zhu, W.; Xu, G.-L.; La Monaca, A.; Savoie, S.; Girard, G.; Vijh, A.; Demers, H.; Perea, A.; Delaporte, N., et al. *Advanced Energy Materials* **2020**, 10, (32), 2001497.

(13) Wu, J.; Yuan, L.; Zhang, W.; Li, Z.; Xie, X.; Huang, Y. *Energy & Environmental Science* **2021**, 14, (1), 12-36.

(14) Kaboli, S.; Demers, H.; Paolella, A.; Darwiche, A.; Dontigny, M.; Clément, D.; Guerfi, A.; Trudeau, M. L.; Goodenough, J. B.; Zaghib, K. *Nano Letters* **2020**, 20, (3), 1607-1613.

(15) Kaboli, S.; Noel, P.; Clément, D.; Demers, H.; Paolella, A.; Bouchard, P.; Trudeau, M. L.; Goodenough, J. B.; Zaghib, K. *Science Advances* **2020**, 6, (50), eabd5708.

(16) Podor, R.; Bouala, G. I. N.; Ravaux, J.; Lautru, J.; Clavier, N. *Materials Characterization* **2019**, 151, 15-26.

(17) Torres, E. A.; Ramírez, A. J., In situ scanning electron microscopy. In Science and Technology of Welding and Joining, Taylor & Francis: **2011**; Vol. 16, pp 68-78.

(18) Golozar, M.; Paolella, A.; Demers, H.; Bessette, S.; Lagacé, M.; Bouchard, P.; Guerfi, A.; Gauvin, R.; Zaghib, K. *Communications Chemistry* **2019**, 2, (1), 131.

(19) Jain, A.; Ong, S. P.; Hautier, G.; Chen, W.; Richards, W. D.; Dacek, S.; Cholia, S.; Gunter, D.; Skinner, D.; Ceder, G., et al. *APL Materials* **2013**, 1, (1), 011002.

(20) Feng, X.; Ren, D.; He, X.; Ouyang, M. *Joule* **2020**, 4, (4), 743-770.

(21) Liu, X.; Yin, L.; Ren, D.; Wang, L.; Ren, Y.; Xu, W.; Lapidus, S.; Wang, H.; He, X.; Chen, Z., et al. *Nature Communications* **2021**, 12, (1), 4235.

(22) Cheng, Q.; Li, A.; Li, N.; Li, S.; Zangiabadi, A.; Li, T.-D.; Huang, W.; Li, A. C.; Jin, T.; Song, Q., et al. *Joule* **2019**, 3, (6), 1510-1522.